

Alma Mater Studiorum Università di Bologna
Archivio istituzionale della ricerca

The Hubble Space Telescope UV Legacy Survey of Galactic Globular Clusters. XV. the Dynamical Clock:
Reading Cluster Dynamical Evolution from the Segregation Level of Blue Straggler Stars

This is the final peer-reviewed author's accepted manuscript (postprint) of the following publication:

Published Version:

Availability:

This version is available at: <https://hdl.handle.net/11585/670314> since: 2019-02-21

Published:

DOI: <http://doi.org/10.3847/1538-4357/aac01c>

Terms of use:

Some rights reserved. The terms and conditions for the reuse of this version of the manuscript are specified in the publishing policy. For all terms of use and more information see the publisher's website.

This item was downloaded from IRIS Università di Bologna (<https://cris.unibo.it/>).
When citing, please refer to the published version.

(Article begins on next page)

This is the final peer-reviewed accepted manuscript of:

F. R. Ferraro et al., *The Hubble Space Telescope UV Legacy Survey of Galactic Globular Clusters. XV. The Dynamical Clock: Reading Cluster Dynamical Evolution from the Segregation Level of Blue Straggler Stars*, 2018, *The Astrophysical Journal*, Volume 860, Article 36.

The final published version is available online at: <https://doi.org/10.3847/1538-4357/aac01c>

Rights / License:

The terms and conditions for the reuse of this version of the manuscript are specified in the publishing policy. For all terms of use and more information see the publisher's website.

This item was downloaded from IRIS Università di Bologna (<https://cris.unibo.it/>)

When citing, please refer to the published version.

The Hubble Space Telescope UV Legacy Survey of Galactic Globular Clusters - XV. The dynamical clock: reading cluster dynamical evolution from the segregation level of blue straggler stars

F.R. Ferraro^{1,2}, B. Lanzoni^{1,2}, S. Raso^{1,2}, D. Nardiello³, E. Dalessandro², E. Vesperini⁴, G. Piotto³, C. Pallanca^{1,2}, G. Beccari⁵, A. Bellini⁶, M. Libralato⁶, J. Anderson⁶, A. Aparicio^{7,8}, L.R. Bedin⁹, S. Cassisi¹⁰, A.P. Milone³, S. Ortolani³, A. Renzini⁹, M. Salaris¹¹, R.P. van der Marel^{6,12}

¹ *Dept. of Physics and Astronomy, University of Bologna, Via Gobetti 93/2, Bologna, Italy*

² *INAF Osservatorio di Astrofisica e Scienza dello Spazio di Bologna, Via Gobetti 93/3, Bologna, Italy*

³ *Dept. of Physics and Astronomy Galileo Galilei, University of Padova, Vicolo dell'Osservatorio 3, I-35122 Padova, Italy*

⁴ *Dept. of Astronomy, Indiana University, Bloomington, IN, 47401, USA*

⁵ *European Southern Observatory, Karl-Schwarzschild-Strasse 2, 85748 Garching bei München, Germany*

⁶ *Space Telescope Science Institute, 3700 San Martin Drive, Baltimore, MD 21218, USA.*

⁷ *Instituto de Astrofisica de Canarias, E-38200 La Laguna, Tenerife, Canary Islands, Spain*

⁸ *Department of Astrophysics, University of La Laguna, E-38200 La Laguna, Tenerife, Canary Islands, Spain*

⁹ *INAF-Osservatorio Astronomico di Padova, Vicolo dell'Osservatorio 5, I-35122 Padova, Italy*

¹⁰ *Osservatorio Astronomico di Teramo, Via Mentore Maggini s.n.c., I-64100 Teramo, Italy*

¹¹ *Astrophysics Research Institute, Liverpool John Moores University, Liverpool Science Park, IC2 Building, 146 Brownlow Hill, Liverpool L3 5RF, UK*

¹² *Center for Astrophysical Sciences, Department of Physics & Astronomy, Johns Hopkins University, Baltimore, MD 21218, USA*

ABSTRACT

The parameter A^+ , defined as the area enclosed between the cumulative radial distribution of blue straggler stars (BSSs) and that of a reference population, is a powerful indicator of the level of BSS central segregation. As part of the Hubble Space Telescope UV Legacy Survey of Galactic globular clusters (GCs), here we

present the BSS population and the determination of A^+ in 27 GCs observed out to about one half-mass radius. In combination with 21 additional clusters discussed in a previous paper this provides us with a global sample of 48 systems (corresponding to $\sim 32\%$ of the Milky Way GC population), for which we find a strong correlation between A^+ and the ratio of cluster age to the current central relaxation time. Tight relations have been found also with the core radius and the central luminosity density, which are expected to change with the long-term cluster dynamical evolution. An interesting relation is emerging between A^+ and the ratio of the BSS velocity dispersion relative to that of main sequence turn-off stars, which measures the degree of energy equipartition experienced by BSSs in the cluster. These results provide further confirmation that BSSs are invaluable probes of GC internal dynamics and A^+ is a powerful dynamical clock.

Subject headings: stars: blue stragglers — stars: kinematics and dynamics — globular clusters: individual (NGC 362, NGC 1261, NGC 1851, NGC 2298, NGC 2808, NGC 4590, NGC 5286, NGC 5986, NGC 6093, NGC 6144, NGC 6341, NGC 6397, NGC 6496, NGC 6535, NGC 6541, NGC 6584, NGC 6624, NGC 6637, NGC 6652, NGC 6681, NGC 6717, NGC 6723, NGC 6779, NGC 6934, NGC 6981, NGC 7078, NGC7089) — methods: observational — techniques: photometric

1. Introduction

Blue straggler stars (BSSs) appear as a sparse group of stars lying along an extrapolation of the main sequence (MS), at brighter magnitudes and bluer colors than the MS turnoff (MS-TO), in the color-magnitude diagram (CMD) of old stellar populations (e.g., Sandage 1953; Ferraro et al. 1992, 1993, 1997, 2004, 2006a; Lanzoni et al. 2007a,b; Leigh et al. 2007; Moretti et al. 2008; Dalessandro et al. 2008; Beccari et al. 2011; Simunovic & Puzia 2016). Their location in the CMD and a growing set of additional observational evidence (Shara et al. 1997; Gilliland et al. 1998; Ferraro et al. 2006b; Fiorentino et al. 2014) suggest that they are more massive than any cluster star with active thermonuclear burnings. In the absence of any recent star-formation event, the origin of BSSs must be sought by exploring mechanisms that are able to increase the initial mass of single stars. Two main BSS formation channels have been identified so far: (1) mass-transfer in binary systems, possibly up to the complete coalescence of the two companions (McCrea 1964), and (2) stellar mergers resulting from direct collisions (Hills & Day 1976). The relative importance of each process likely depends on the physical properties of the parent cluster (e.g., Davies et al. 2004; Sollima et al. 2008; Chen & Han 2009; Knigge et al. 2009; Ferraro et al. 2009; Leigh et al.

2013; Chatterjee et al. 2013a; Sills et al. 2013), and there is no way at present to properly quantify this. Moreover, a few indications suggest that both channels can be active with comparable efficiency within the same cluster (Ferraro et al. 2009; Dalessandro et al. 2013; Simunovic et al. 2014; Xin et al. 2015). Irrespective of their formation mechanism, BSSs are a population of heavy objects ($\sim 1\text{-}1.6M_{\odot}$) orbiting in a sea of lighter stars (the average stellar mass in an old GC is $\langle m \rangle \sim 0.3M_{\odot}$) with a density distribution that varies by several orders of magnitude between the center and the periphery of the host cluster (e.g., McLaughlin & van der Marel 2005; Miocchi et al. 2013; Baumgardt 2017). For this reason BSSs can be used as powerful *gravitational probe particles* to investigate key dynamical processes (such as mass segregation) characterizing the dynamical evolution of star clusters (e.g., Ferraro et al. 2009, 2015, Dalessandro et al. 2013; Simunovic et al. 2014). The signature of these processes, in fact, can remain imprinted in some BSS observational features. This is the core concept of the so-called *dynamical clock* (see (Ferraro et al. 2012, hereafter F12) and subsequent refinements in Alessandrini et al. 2016 and Lanzoni et al. 2016, hereafter L16).

F12 demonstrated that the observed morphology of the BSS normalized radial distribution¹ (hereafter BSS-nRD) is shaped by the action of dynamical friction (DF), which drives the objects more massive than the average toward the cluster center, with an efficiency that decreases with increasing radial distance. Thus, because of DF, a peak followed by a minimum (a sort of BSS “zone of avoidance”; see also Mapelli et al. 2004, 2006) is expected to appear at small radii in the BSS-nRD ratio and then propagate to larger and larger distances from the cluster center as a function of time. Accordingly, F12 identified the observed shape of the BSS-nRD as a “dynamical clock” able to measure the level of dynamical evolution experienced by a cluster, and the radial location of the distribution minimum (r_{\min}) as the clock hand. This feature, in fact, marks the most external region of the system that has been significantly affected by DF, and its distance from the center therefore depends on how much a cluster is dynamically evolved. This parameter, expressed in units of the cluster core radius (r_{\min}/r_c), was used by F12 to define families and sub-families of GCs in different stages of their dynamical evolution (i.e., with different dynamical ages), all having, however, the same chronological age ($t \sim 12\text{-}13$ Gyr).

By using direct N-body simulations, Alessandrini et al. (2016) proposed an alternative and binning-independent parameter (A^+) to characterize the progressive central segregation of BSSs. A^+ is defined as the area enclosed between the cumulative radial distribution of BSSs and that of a reference (and lighter) population. L16 measured this quantity within one half-mass radius (r_h) for a sample of GCs and found a well-defined correlation between

¹The “normalized BSS distribution” (Ferraro et al. 1993) is defined as the ratio between the fraction of BSSs sampled in any adopted radial bin and the fraction of cluster light sampled in the same bin.

A^+ and the central relaxation time t_{rc} of the system. The new parameter A^+ also strongly correlates with the hand of the dynamical clock, r_{\min} (see Figure 2 in L16). This is not obvious *a priori*, since the definitions of the two parameters are completely independent. The evidence that, instead, they are mutually linked through a tight and direct correlation indicates that they describe the same phenomenon, i.e., the progressive central segregation of BSSs due to the action of DF. These actually are different ways of measuring the same process: as clusters get dynamically older, DF progressively brings in BSSs from increasingly larger distances from the center (thus generating a BSS-nRD minimum at increasingly larger values of r_{\min}); correspondingly, BSSs accumulate toward the cluster center (and the value of A^+ increases). From an operational point of view, A^+ provides some advantages with respect to the method based on r_{\min} : (i) A^+ is easier to measure, since it does not require us to sample the entire radial extension of the surveyed clusters; (ii) it does not depend on (somewhat arbitrary) assumptions about the radial binning; and (iii) it describes a high-signal region where DF is accumulating BSSs (instead of a low signal region, as the zone of avoidance). The latter property should also help us to reproduce the observations through numerical simulations. Indeed, detecting the minimum of the BSS-nRD is known to be a difficult task (e.g., Miocchi et al. 2015), since BSSs are an intrinsically scarce population and they rapidly become less and less common in the external regions of a cluster. The correct identification of r_{\min} is then critically dependent on the choice of the radial binning, since adopting intervals that are too wide tends to wipe out the feature, while bins that are too narrow generate noisy distributions because of the decreasing number of sampled objects. Thus, it is not surprising that blind automatic searches for r_{\min} and its outward migration in numerical simulations have been unsuccessful (e.g., Miocchi et al. 2015; Hypki & Giersz 2017). While this difficulty should not be confused with a lack of effectiveness for r_{\min} to trace the dynamical evolution of GCs, the parameter A^+ should simplify the reproducibility of the observations via numerical simulations (which already succeed in finding the central peak and the central BSS segregation; Miocchi et al. 2015; Hypki & Giersz 2017).

As part of the HST UV Legacy Survey of GCs (Piotto et al. 2015) series, this paper presents the determination of A^+ in 27 systems that have been observed out to $\sim 1r_h$ (see Sect. 4). In combination with the sample of L16, this provides us with a measure of A^+ in roughly 32% of the entire GC population in the Milky Way. For this sample we find a strong correlation between A^+ and the number of central relaxation times that have occurred in each cluster since formation. A correlation between the level of BSS central segregation (as quantified by A^+) and the degree of energy equipartition experienced by BSSs in the cluster (as measured by the velocity-dispersion ratio of BSSs and MS-TO stars) is also found for the 14 GCs in common with Baldwin et al. (2016). The paper is organized as follows: in Section 2 we present the UV approach to the study of BSSs and the photometric database

used; in Section 3 we describe the BSS selection criteria; in Section 4 we determine A^+ and discuss the results.

2. The photometric database and data analysis

2.1. The UV approach

Since the optical emission of old stellar systems is dominated by cool bright giants, the systematic acquisition of complete samples of BSSs at optical wavelengths is an intrinsically difficult task even with HST (Ferraro et al. 1997, 1999, 2015). Instead, BSS searches are particularly effective in the UV, where these stars appear among the brightest objects in a GC and red giant branch (RGB) stars are particularly faint. Thus, the usual problems associated with photometric blends and crowding in the high-density central regions of GCs are minimized, and BSSs can be reliably recognized and easily separated from both other evolved and unevolved populations at UV wavelengths. Based on these considerations, several years ago we first promoted the so-called *UV route to the study of BSSs in GCs* (see Ferraro et al. 1997, 1999, 2001, 2003), an approach that allowed us to derive complete samples of BSSs even in the central regions of the densest systems (see Lanzoni et al. 2007a,b,c; Dalessandro et al. 2008, 2009; Sanna et al. 2012, 2014; Contreras Ramos et al. 2012; Parada et al. 2016). Now, the dataset acquired in the HST UV Legacy Survey of GCs (GO-13297; Piotto et al. 2015) allows us to extend this approach to a significant number of additional clusters. As a first step, in Raso et al. (2017, hereafter, R17) we presented the BSS populations obtained from these data in four GCs (namely, NGC 2808, NGC 6388, NGC 6541, NGC 7078), and compared them to the optical selections previously published for these same systems, clearly demonstrating the great advantage of a *UV-guided* search for BSSs relative to *optical-guided* hunts. The discussion of the BSS properties in terms of luminosity function, population ratios, and correlations with the parent cluster properties for the entire sample of GCs observed in the survey will be presented and discussed in a forthcoming paper (Ferraro et al. 2018, in preparation). Here we focus on the 27 systems for which the observations cover radial distances out to $\sim 1r_h$ (see Sect. 4).

2.2. The photometric database

An overview of the HST UV Legacy Survey of GCs is presented in Piotto et al. (2015)². Here we summarize a few characteristics that are particularly relevant for the study of BSSs. Several images have been obtained for each cluster in the F275W, F336W and F438W bands with the UVIS channel of the WFC3. WFC3/UVIS consists of two chips, each of 4096×2051 pixels, with a pixel scale of $0.04''$, resulting in a total field of view of $\sim 162'' \times 162''$. In each band, different pointings were dithered by several pixels, and in some cases they were also rotated by $\sim 90^\circ$, to allow an optimal subtraction of CCD defects, artifacts, charge loss and false detections. All the images have been corrected for the effect of poor charge transfer efficiency following Anderson & Bedin (2010). In the following we briefly describe the main novelty of the *UV-guided* photometric approach here adopted (see also R17), with respect to the early data releases based on an *optical-guided* reduction of the images (see, e.g., Soto et al. 2017).

The photometric catalogs were obtained using the software described by Anderson et al. (2008) and adapted to WFC3 images. Briefly, for each image we obtained an ad-hoc array of PSFs by perturbing the tabulated static PSFs³, to properly take into account both the spatial and the temporal PSF variations. To extract the photometric catalogs from each individual exposure by using the adopted arrays of PSFs we then ran the software `img2xym_wfc3uv`, which has been optimized for UVIS/WFC3 data by Jay Anderson and is similar to the `img2xym_WFC` program (Anderson et al. 2008). After correcting the stellar positions for geometric distortion (Bellini & Bedin 2009; Bellini et al. 2011), we determined the transformations between the single-exposure catalogs. Finally, to take full advantage of the reduced crowding conditions at UV wavelengths, we chose to perform the finding procedure on the F275W and F336W images (see also R17) and then measured stars in all the individual exposures. To this end, we used the FORTRAN program `kitchen_sync`, described by Anderson et al. (2008) and adapted to WFC3 images. The final product is an astrophotometric catalog containing the positions and the F275W, F336W, and F438W magnitudes of all the stars found. For a first-guess differential reddening correction and field decontamination, information about reddening and proper motions have been added to all the stars in common with the catalogs published in the intermediate release⁴ (Piotto et al. 2015) and available upon request at the web page <http://groups.dfa.unipd.it/ESPG/treasury.php>.

²<http://groups.dfa.unipd.it/ESPG/treasury.php>

³<http://www.stsci.edu/~jayander/STDPSFs/>

⁴Since these latter are based on an *optical-guided* data reduction, reddening and proper motion measures are available only for a sub-sample of the stars in our final catalogs.

3. The BSS selection in UV-CMDs

R17 identified the purely UV ($m_{\text{F275W}}, m_{\text{F275W}} - m_{\text{F336W}}$) CMD as the ideal diagram for BSS selection, since this population is clearly distinguishable from the other evolutionary sequences (see their Figure 1). In particular, (1) along with the hottest extension of the horizontal branch (HB), BSSs appear to be the brightest objects in this CMD, while most of the RGB stars are significantly fainter; (2) BSSs define a clean sequence populating a strip that has a vertical extension of ~ 3 magnitudes and is ~ 2 magnitudes wide in color; (3) BSSs are clearly distinguishable from MS-TO and sub-giant branch (SGB) stars.

To perform a homogeneous selection of BSSs in clusters with different values of distance, reddening and metallicity, we adopted the procedure suggested by R17, defining a “normalized” CMD (hereafter n-CMD) where the magnitudes and the colors of all the measured stars in a given cluster are arbitrarily shifted to locate the MS-TO at $m_{\text{F275W}}^* = 0$ and $(m_{\text{F275W}} - m_{\text{F336W}})^* = 0$. Since the morphology of the MS-TO and the SGB region changes as a function of metallicity, and because the surveyed GCs have quite different iron abundances (ranging from $[\text{Fe}/\text{H}] = -0.4$ for NGC 6624, to $[\text{Fe}/\text{H}] = -2.4$ for NGC 7078), we adopted the following procedure to determine the necessary shifts for a proper normalization of the CMDs:

1. While the updated determination of precise proper motions for all the clusters in the survey is in progress, here we used the currently available measurements for a first-order identification of field stars in the most contaminated systems. Proper motions have been determined over a ~ 7 -8 yr time-baseline using the Advanced Camera for Surveys (ACS) Globular Cluster Survey data (GO-10775; Sarajedini et al. 2007) as first-epoch observations and the new WFC3 UV positions as the second epoch. To separate cluster members from field stars, we built the vector point diagrams (VPDs) plotting all the available displacement measures in each cluster. We thus used an iterative σ -rejection procedure⁵ to distinguish cluster members, which are well-grouped around the VPD center, from field contaminants, which generally exhibit a much more scattered distribution (see also King et al. 1998; Bedin et al. 2003; Bellini et al. 2009, 2014; Milone et al. 2012; Massari et al. 2015; Cadelano et al. 2017; Soto et al. 2017). For illustration purposes we show in Figure 1 the VPDs of three clusters. All stars with no displacement information have been conservatively retained as members in the

⁵Starting from a first-guess circle of radius r_i in the VPD, we selected all the enclosed stars and determined their dispersion along the two axes (dx and dy). At the following step, the new selection radius is defined as $r = 4 \times \sigma_{xy}$, where $\sigma_{xy} = \sqrt{dx^2 + dy^2}$. The final selection radius is then obtained when convergence is reached (typically, after five iterations).

following analysis.

2. All the stars for which we have color-excess determinations available were then corrected for differential reddening following the approach described, e.g., in Milone et al. (2012, 2017).
3. The available clusters were divided into three groups according to their metallicity: metal-poor, with $[\text{Fe}/\text{H}] < -2$, metal-intermediate, with $-2 < [\text{Fe}/\text{H}] < -1$, and metal-rich, with $[\text{Fe}/\text{H}] > -1$.
4. For each group, a 12 Gyr-old isochrone of appropriate metallicity was adopted from the BASTI database (Pietrinferni et al. 2006) and was plotted for reference in the n-CMD, i.e., in the CMD with the MS-TO located at (0,0).
5. The stellar magnitudes and colors in each cluster were then shifted to match the appropriate reference isochrone.

For the sake of illustration, Figure 2 shows the n-CMD zoomed in the MS-TO region for three clusters representative of the three adopted metallicity groups (see labels). The observed sequences at the MS-TO/SGB level nicely agree with the shape of the appropriate isochrone.

By construction, BSSs are expected to populate the same region in the n-CMDs, Hence they can be selected in a homogeneous way by defining a unique selection box (see the upper-left panel in Figure 3). Here we adopt the same boundaries defined in R17, which have been designed to include the bulk of the BSS population in all the clusters, independent of their metallicity (note that the BSS sequence slightly moves from blue to red for increasing iron content).⁶ As discussed in R17, the bright edge of the BSS selection box is needed to distinguish very luminous BSSs from stars populating the blue portion of the HB (when present). Since the HB morphology is expected to vary (primarily) as a function of the metallicity, different bright boundaries of the BSS selection boxes were adopted for the three

⁶ For sake of completeness here we report the equations of the lines delimiting the BSS box (see the first panel in Figure 3). The two parallel strips, designed to include the bulk of the BSS population independently of the cluster metallicity, have equations: $m_{\text{F}275\text{W}}^* = 3.86 \times (m_{\text{F}275\text{W}} - m_{\text{F}336\text{W}})^* - 1.48$ and $m_{\text{F}275\text{W}}^* = 3.86 \times (m_{\text{F}275\text{W}} - m_{\text{F}336\text{W}})^* + 0.56$. The red boundary, located at $(m_{\text{F}275\text{W}} - m_{\text{F}336\text{W}})^* = -0.05$, is needed to exclude the objects populating the “plume” above the MS-TO, which is visible in the most massive high-density clusters and is essentially due to photometric blends. The bottom edge, which separates faint BSSs from MS-TO stars, is set at more than $5\text{-}\sigma$ from the typical mean color of the MS-TO distribution and has equation: $m_{\text{F}275\text{W}}^* = -4 \times (m_{\text{F}275\text{W}} - m_{\text{F}336\text{W}})^* - 0.58$. Note that in some cases a few objects lying close to the selection box boundaries have been excluded to minimize the presence of contaminating stars. This has no impact on the discussed results.

metallicity groups. Figures 3-5 show the BSS sample selected in the 27 GCs discussed in the paper.

For meaningful conclusions, the radial distribution of BSSs needs to be compared with that of a population of normal cluster stars tracing the overall density profile of the system (hereafter, REF population). In order to measure the A^+ parameter as accurately as possible, we choose to use MS stars around the MS-TO level. The adopted REF population selection box (see Figures 3-5) is delimited in magnitude between $m_{F275W}^* = -0.45$ and $m_{F275W}^* = 0.4$ and in color between $(m_{F275W} - m_{F336W})^* = 0.2$ and the line $m_{F275W}^* = -6.30 \times (m_{F275W} - m_{F336W})^* - 0.62$. This portion of the CMD turns out to provide the ideal REF population, since it includes several hundred stars and therefore is negligibly affected by statistical fluctuations. It is also expected to be poorly affected by the possible presence of binary systems, since the number of single MS-TO stars is largely dominant within the adopted box.

4. Results and Discussion

To measure the level of BSS segregation in the surveyed clusters we used the parameter A^+ , which is defined (see Alessandrini et al. 2016) as the area enclosed between the cumulative radial distribution of BSSs, $\phi_{\text{BSS}}(x)$, and that of a reference (lighter) population, $\phi_{\text{REF}}(x)$:

$$A^+(x) = \int_{x_0}^x \phi_{\text{BSS}}(x') - \phi_{\text{REF}}(x') dx', \quad (1)$$

where x_0 and x are the innermost and the outermost distances from the cluster center considered in the analysis. As discussed in previous papers, the parameter A^+ has been designed to describe the sedimentation-type process that progressively makes BSSs sink toward the cluster center, thus tracing the level of dynamical evolution of the system. In principle, then, the measure of A^+ requires only that the observations cover the cluster region most sensitive to the BSS segregation (i.e. the central region), and that this be large enough to allow a sufficient sampling of the cumulative radial distributions. Moreover, to compare values of A^+ obtained in GCs with different structures and sizes, this parameter should be determined within equivalent radial portions in each system. Determining the exact extension of this portion is a complex task, since it depends on the properties of the cluster and of its stellar populations (for instance, the number of BSSs found within one core radius from the center can be a very small or a relatively large number, depending on the cluster). Following L16 we measure A^+ out to one half-mass radius (hereafter, A_{rh}^+) and we express distances on a logarithmic scale to enhance the sensitivity of the parameter to the segregation of BSSs, which is predominant in the central regions of each system (hence

$x = \log(r/r_h)$ in the above equation).

Our HST-WFC3 data covers approximately the innermost 80''-85'' in each surveyed cluster. This is large enough to sample the entire half-mass radius in 22 of the clusters. We also added to the sample four clusters (namely, NGC 4590, NGC 6144, NGC 6496 and NGC 6723) for which the available data cover between $\sim 90\%$ and 98% of r_h . We also added NGC 6397, which is known to be a post-core collapse cluster and therefore is expected to belong to the family of dynamically-old GCs (Family III as defined in F12) and which has a BSS population highly segregated in the central regions. Our data sample ~ 30 core radii in this cluster, and based on the n-RDs discussed in F12, this is a large enough distance for a proper study of BSS segregation. In fact, Figures 2 and 3 in F12 clearly show that the region where the BSS-nRD shows a central peak (which is the signature of BSS sedimentation) is of the order of a few core radii in all clusters. Hence, the total sample extracted from the HST UV Legacy Survey of GCs for the present analysis amounts to 27 objects. To increase the size of the sample, we also take into account 21 GCs from L16. The parameter A^+ in L16 has been determined from a combination of UV HST observations and complementary wide-field optical data from the ground able to sample the entire half-mass radius region of each system. To minimize the risk of stellar blends mimicking BSSs at optical wavelengths (see an example in Figures 5 and 6 in Lanzoni et al. 2007b), in L16 only the brightest portion of the BSS distribution has been taken into account. Hence, for consistency, in the present analysis we consider only BSSs with $m_{F275W}^* < -1.0$. This selection corresponds to including only the most massive tail of the BSS population, thus maximizing the sensitivity of the A^+ parameter to the mass-segregation effect. Although caution is needed in deriving BSS masses from their luminosity distribution (see Geller & Mathieu 2012), the adopted magnitude cut roughly corresponds to selecting BSSs that are more massive than $\sim 1.2M_\odot$. The cumulative radial distributions of BSS and REF populations here determined for the 27 investigated clusters are shown in Figures 6-8, and the corresponding values of $A_{r_h}^+$ are labeled in each panel and listed in Table 1. The primary source of uncertainty on A^+ is the relatively small-number statistics of the BSS sample in each system. To estimate the errors on A^+ (see Table 1) we therefore used a jackknife bootstrapping technique (Lupton 1993).⁷

Since the adopted BSS and REF populations have different magnitude limits, they could be characterized by different levels of completeness, which, in turn, could impact the value of $A_{r_h}^+$. Hence, we performed artificial star experiments to estimate the photometric completeness of the two populations in some of the most massive (hence most crowded) clusters with different central densities. In the worst cases of the intermediate density systems

⁷For sake of consistency, we re-evaluated the errors on A^+ of the L16 sample using the same technique.

(as NGC 2808) the completeness of the BSS and REF populations is always larger than $\sim 90\%$, with the only exception being the faintest MS-TO stars at $r < 15''$, for which it decreases to $\sim 80\%$. In the most compact clusters (as M15) the selected populations are complete at more than 90% for $r > 30''$, while the completeness decreases to 80% and 70-75% at the faintest boundary of the MS-TO selection box for $15'' < r < 30''$ and $r < 15''$, respectively. We redetermined the value of A_{rh}^+ from 1000 random realizations of the two population samples corrected for the estimated incompleteness levels. The mean value and dispersion of the resulting A_{rh}^+ distributions are well within the uncertainties estimated with the jackknife bootstrapping technique, thus indicating that the photometric incompleteness of the adopted samples does not affect the present analysis.

To investigate the connection between the BSS segregation level and the dynamical status of the parent cluster, we studied the relation between the measured values of A_{rh}^+ and the dynamical age of the system quantified by the number of current central relaxation times (t_{rc}) that have occurred since the epoch of cluster formation (t_{GC}): $N_{\text{relax}} = t_{GC}/t_{rc}$. Because all Galactic GCs have approximately the same age, this is simply an alternative way of illustrating the connection between A^+ and the dynamical evolution experienced by a cluster, with respect to the direct comparison between A^+ and t_{rc} adopted in previous works (F12, L16 and R17). Indeed, to keep the sources of uncertainty at a minimum, for all the program clusters we assumed the same average age ($t_{GC} = 12$ Gyr from the compilation of Forbes & Bridges 2010). Note however that adopting individual age estimates for each cluster does not change the result. The central relaxation times have been empirically estimated as in equation (10) of Djorgovski (1993), adopting $0.3M_{\odot}$ as average stellar mass, $M/L_V = 2$ as V -band mass-to-light ratio, the integrated V magnitudes listed in Harris (1996), and the structural parameters listed in Table 1.

The nice correlation in Figure 9 clearly shows that A^+ is a powerful indicator of cluster dynamical evolution. The most dynamically evolved cluster in the sample is NGC 6397, and the five objects with the next largest values of A_{rh}^+ (namely, M30, NGC 1851, NGC 6652, NGC 6681, and NGC 6624) are all post-core collapse or high-density systems. The present study also increased the number of clusters showing a modest level of dynamical evolution. In fact we count at least 6-7 GCs with extremely low values of A_{rh}^+ (< 0.05 - 0.06). Interestingly, we also find similarly small values for other objects not included in the present study (as NGC 5053 and NGC 6809) because the WFC3 field of view does not entirely sample their half-mass radius. This suggests that they may also belong to this class, although more radially extended observations are needed. Hence, a significant fraction (possibly $\sim 10\%$) of the Galactic GC population could still be relatively unevolved dynamically.

The best-fit relation to the observed points plotted in Figure 9 is:

$$\log N_{\text{relax}} = 5.1(\pm 0.5) \times A_{rh}^+ + 0.79(\pm 0.12) \quad (2)$$

with a scatter of 0.47 and a high statistical significance: the Spearman rank correlation coefficient is $\rho = 0.82$, and the Pearson correlation coefficient is $r = 0.85$, indicating a strong linear correlation between the two parameters. The relation remains the same even if NGC 6397 which has the largest value of A_{rh}^+ , and/or the four GCs that are not sampled all the way out to r_h are excluded from the analysis. On one hand, this new relation is obtained from $\sim 1/3$ of the total GC population of the Milky Way and thus definitely consolidates the idea that the segregation level of BSSs can be used to evaluate the dynamical evolution experienced by the parent cluster. On the other hand, the scatter of this relation may indicate that further refinements should be used to measure A_{rh}^+ , and, more likely, that the empirical values of t_{rc} are crude approximations of the true relaxation times of Galactic GCs (as discussed, e.g., by Chatterjee et al. 2013b from dedicated Monte Carlo simulations). It is also worth noticing that the current estimates of t_{rc} are still largely based on cluster parameters derived from surface brightness profiles, which could be biased by the presence of few bright stars. In a future paper we will present star count profiles for all the clusters in the HST UV Legacy Survey of GCs, from which accurate values of the central density, core and half-mass radii, and concentration parameter will be derived, and new central relaxation times will be estimated. This might possibly reduce the scatter and provide a refinement of the proposed relation. The scatter notwithstanding, our analysis fully confirms that this is the correct route for a proper description of the dynamical evolution of star clusters. The calibration of the relation via N-body or Monte Carlo simulations requires that all the (known) ingredients (such as dark remnants, primordial binaries, etc.) are taken into account. Indeed preliminary N-body simulations (Alessandrini et al. 2016) have shown how the inclusion of dark remnants can significantly change the BSS segregation timescale in simulated clusters, hence caution should be exercised when calibrating these observables via simulations of simplified models.

To further investigate the solidity of the A^+ parameter as dynamical aging indicator we also studied the dependence on A^+ of two physical parameters that are expected to change with the long-term dynamical evolution of the cluster. Figure 10 shows the behaviour of the core radius (r_c) and the central luminosity density (ρ_0 , both from Harris 1996) as a function of A^+ . The well-defined trends shown in the figure, with r_c decreasing and ρ_0 increasing with A_{rh}^+ (i.e., with increasing dynamical age), nicely match the expectations. The tight and strong detected relations, although somehow predictable on the basis of the result shown in Figure 9, fully confirm the eligibility of the A^+ parameter as dynamical aging indicator.

Baldwin et al. (2016) measured the proper motions of 598 BSSs across 19 GCs, and

inferred the ratio (α) of the velocity dispersion of BSSs (σ_{BSS}) relative to that of stars near the top of the MS ($\sigma_{\text{MS-TO}}$), which is a measure of BSS equipartition (see their equation 3). Figure 11 compares this parameter with our measurement of BSS mass segregation for the 14 GCs in common between the two samples. The best-fit relation is

$$\alpha \equiv \frac{\sigma_{\text{BSS}}}{\sigma_{\text{MS-TO}}} = -0.62(\pm 0.23) \times A_{rh}^+ + 1.01(\pm 0.06) \quad (3)$$

indicating a weak anti-correlation at $\sim 3\sigma$ confidence. The size and the significance of the correlation are strengthened upon omission of NGC 6397 (the cluster with the largest value of A_{rh}^+ in Figure 11), which has the most uncertain velocity dispersion in Baldwin et al. (2016), on account of their measuring only 10 BSSs. The Spearman rank correlation coefficient is then $\rho = -0.39$, and the Person correlation coefficient is $r = -0.38$. The relation indicates that when $A_{rh}^+ = 0$, then $\alpha \sim 1$. So when there not yet been sufficient time for mass segregation to develop, no energy equipartition has developed yet either. These results imply, as expected, that as mass segregation develops, so does a certain level of energy equipartition ($\sigma \propto M^{-\eta}$, where M is the stellar mass and η trends over time from 0 to a maximum value of $\approx 0.1-0.2$, with $\eta = 0.5$ corresponding to complete equipartition; Trenti & van der Marel 2013). These results further confirm our physical understanding of the dynamical evolution of GCs, as well as our earlier arguments that A^+ can be used as the “clock hand” of a dynamical chronometer.

We thank the anonymous referee for useful comments that contributed to improve the presentation of the paper. FRF acknowledges the ESO Visitor Programme for the support and the warm hospitality at the ESO Headquarter in Garching (Germany) during the period when most of this work was performed. D.N, S.O. and G.P. acknowledge partial support by the Università degli Studi di Padova, Progetto di Ateneo CPDA141214 “Towards understanding complex star formation in Galactic globular clusters” and by INAF under the program PRIN-INAF2014. APM acknowledges support by the European Research Council through the ERC-StG 2016 project 716082 ‘GALFOR’. JA and AB acknowledge the support of STScI Grant GO-13297.

REFERENCES

- Alessandrini, E., Lanzoni, B., Miocchi, Ferraro, F. R., Vesperini, E. 2016, ApJ, 833, 252
- Anderson, J., Sarajedini, A., Bedin, L. R., et al. 2008, AJ, 135, 2055
- Anderson, J., Bedin L.R., 2010, PASP, 122, 1035

- Bailyn, C. D. 1995, *ARA&A*, 33, 133
- Baldwin, A. T., Watkins, L. L., van der Marel, R. P., et al. 2016, *ApJ*, 827, 12
- Baumgardt, H. 2017, *MNRAS*, 464, 2174
- Beccari, G., Sollima, A., Ferraro, F. R., et al., 2011, *ApJ*, 737, 3.
- Bedin, L. R., Piotto, G., King, I. R., & Anderson, J. 2003, *AJ*, 126, 247
- Bellini, A., Piotto, G., Bedin, L. R., et al. 2009, *A&A*, 493, 959
- Bellini, A., & Bedin, L. R. 2009, *PASP*, 121, 1419
- Bellini, A., Anderson, J., & Bedin, L. R. 2011, *PASP*, 123, 622
- Bellini, A., Anderson, J., van der Marel, R. P., et al. 2014, *ApJ*, 797, 115
- Cadelano, M., Dalessandro, E., Ferraro, F. R., et al. 2017, *ApJ*, 836, 170
- Chatterjee, S., Rasio, F. A., Sills, A., & Glebbeek, E. 2013a, *ApJ*, 777, 106
- Chatterjee, S., Umbreit, S., Fregeau, J. M., & Rasio, F. A. 2013b, *MNRAS*, 429, 2881
- Chen, X., & Han, Z. 2009, *MNRAS*, 395, 1822
- Contreras Ramos, R., Ferraro, F. R., Dalessandro, E., Lanzoni, B., & Rood, R. T. 2012, *ApJ*, 748, 91
- Dalessandro, E., Lanzoni, B., Ferraro, F. R., Vespe, F., Bellazzini, M., Rood, R. T., 2008, *ApJ*, 681, 311.
- Dalessandro, E., Beccari, G., Lanzoni, B., et al. 2009, *ApJS*, 182, 509
- Dalessandro, E., Ferraro, F. R., Massari, D., et al. 2013, *ApJ*, 778, 135
- Davies, M. B., Piotto, G., & de Angeli, F. 2004, *MNRAS*, 349, 129
- Djorgovski, S. 1993, *ASPC*, 50, 373
- Ferraro, F. R., Fusi Pecci, F., & Buonanno, R. 1992, *MNRAS*, 256, 376
- Ferraro, F. R., Fusi Pecci, F., Cacciari, C., 1993, *AJ*, 106, 2324.
- Ferraro, F. R., Paltrinieri, B., Fusi Pecci, F., et al. 1997, *A&A*, 324, 915.
- Ferraro, F. R., Paltrinieri, B., Rood, R. T., & Dorman, B. 1999, *ApJ*, 522, 983

- Ferraro, F. R., D'Amico, N., Possenti, A., Mignani, R. P., & Paltrinieri, B. 2001, *ApJ*, 561, 337
- Ferraro, F. R., Sills, A., Rood, R. T., Paltrinieri, B., & Buonanno, R. 2003, *ApJ*, 588, 464
- Ferraro F. R., Beccari G., Rood, R. T., Bellazzini M., Sills A., Sabbi E., 2004 *ApJ*, 603, 127.
- Ferraro, F. R., Sollima, A., Rood, R. T., Origlia, L., Pancino, E., Bellazzini, M., 2006a, *ApJ*, 638, 433.
- Ferraro, F. R., Sabbi, E., Gratton R., et al. 2006b, *ApJ*, 647, L53.
- Ferraro, F. R., Beccari, G., Dalessandro, E., et al. 2009, *Nature*, 462, 1028
- Ferraro, F. R., Lanzoni, B., Dalessandro, E., et al., 2012, *Nature*, 492, 393 (F12)
- Ferraro, F. R., Lanzoni, B., Dalessandro, E., Mucciarelli, A., & Lovisi, L. 2015, *Ecology of Blue Straggler Stars*, 99
- Fiorentino, G., Lanzoni, B., Dalessandro, E., Ferraro, F. R., Bono, G., Marconi, M., 2014, *ApJ*, 783, 29.
- Forbes, D., Bridges, T., 2010, *MNRAS*, 404, 1203
- Geller, A. M., & Mathieu, R.D. 2011, *AJ*, 144, 54
- Gilliland, R. L., Bono, G., Edmonds, P. D., et al. 1998, *ApJ*, 507, 818
- Harris, W. E. 1996, *AJ*, 112, 1487, 2010 edition
- Hills, J. G., & Day, C. A. 1976, *Astrophys. Lett.*, 17, 87
- Hypki, A., & Giersz, M. 2017, *MNRAS*, 471, 2537
- King, I. R., Anderson, J., Cool, A. M., & Piotto, G. 1998, *ApJ*, 492, L37
- Knigge, C., Leigh, N., & Sills, A. 2009, *Nature*, 457, 288
- Lanzoni, B., Sanna, N., Ferraro, F. R., Valenti, E., Beccari, G., Schiavon, R. P., Rood, R. T., Mapelli, M., Sigurdsson, S., 2007a, *ApJ*, 663, 1040
- Lanzoni, B., Dalessandro, E., Ferraro, F. R., Mancini, C., Beccari, G., Rood, R. T., Mapelli, M., Sigurdsson, S., 2007b, *ApJ*, 663, 267
- Lanzoni, B., Dalessandro, E., Perina, S., et al. 2007c, *ApJ*, 670, 1065

- Lanzoni, B., Ferraro, F. R., Alessandrini, E., Dalessandro, E., Vesperini, E., Raso, S. 2016, *ApJ*, 833, L29 (L16)
- Leigh, N., Sills, A., & Knigge, C. 2007, *ApJ*, 661, 210
- Leigh, N., Knigge, C., Sills, A., et al. 2013, *MNRAS*, 428, 897
- Lupton, R. 1993, Princeton, NJ, Princeton University Press, 1993
- Mapelli, M., Sigurdsson, S., Colpi, M., et al. 2004, *ApJ*, 605, L29
- Mapelli, M., Sigurdsson, S., Ferraro, F. R., et al. 2006, *MNRAS*, 373, 361
- Massari, D., Dalessandro, E., Ferraro, F. R., et al. 2015, *ApJ*, 810, 69
- McCrea, W. H. 1964, *MNRAS*, 128, 147
- McLaughlin, D. E., & van der Marel, R. P. 2005, *ApJS*, 161, 304
- Milone, A. P., Piotto, G., Bedin, L.R., et al. 2012, *A&A*, 540, 41
- Milone, A. P., Piotto, G., Renzini, A. et al. 2017, *MNRAS*, 464, 3636
- Miocchi, P., Lanzoni, B., Ferraro, F. R., et al. 2013, *ApJ*, 774, 151
- Miocchi, P., Pasquato, M., Lanzoni, B., et al. 2015, *ApJ*, 799, 44.
- Moretti, A., de Angeli, F., & Piotto, G. 2008, *A&A*, 483, 183
- Parada, J., Richer, H., Heyl, J. et al. 2016, *The Astroph. J.*, 830, 139
- Pietrinferni, A., Cassisi, S., Salaris, M., & Castelli, F. 2006, *The Astroph. J.*, 642, 797
- Piotto, G., Milone, A. P., Bedin, L. R., et al. 2015, *AJ*, 149, 91
- Raso, S., Ferraro, F. R., Dalessandro, E., et al. 2017, *ApJ*, 839, 64 (R17)
- Sandage A. R., 1953, *AJ*, 58, 61.
- Sanna, N., Dalessandro, E., Lanzoni, B., et al. 2012, *MNRAS*, 422, 1171
- Sanna, N., Dalessandro, E., Ferraro, F. R., et al. 2014, *ApJ*, 780, 90
- Sarajedini, A., Bedin, L. R., Chaboyer, B., et al. 2007, *AJ*, 133, 1658
- Shara, M. M., Saffer, R. A., & Livio, M. 1997, *ApJ*, 489, L59

- Sills, A., Glebbeek, E., Chatterjee, S., & Rasio, F. A. 2013, *ApJ*, 777, 105
- Simunovic, M., Puzia, T. H., & Sills, A. 2014, *ApJ*, 795, L10
- Simunovic, M., & Puzia, T. H. 2016, *MNRAS*, 462, 3401
- Sollima, A., Lanzoni, B., Beccari, G., Ferraro, F. R., & Fusi Pecci, F. 2008, *A&A*, 481, 701
- Soto, M., Bellini, A., Anderson, J., et al. 2017, *AJ*, 153, 19
- Trenti, M., & van der Marel, R. 2013, *MNRAS*, 435, 3272
- Xin, Y., Ferraro, F. R., Lu, P., et al. 2015, *ApJ*, 801, 67

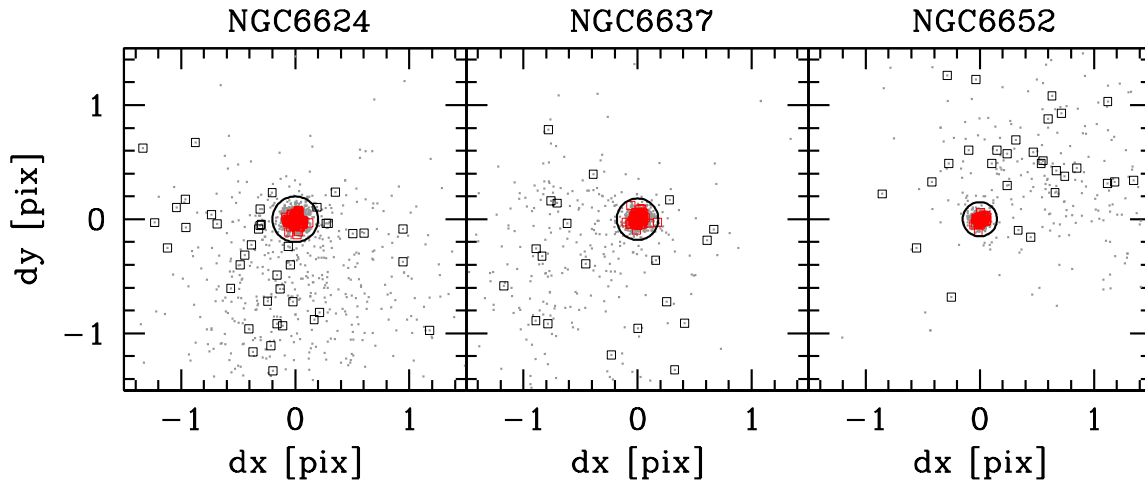


Fig. 1.— Vector-point diagrams (VPDs) for three clusters in the survey (see labels), showing the measured displacements (in ACS/WFC pixels) of stars brighter than the MS-TO level (with $m_{F275W}^* < 0.5$), over a ~ 7 -8 yr time-baseline. All stars within the circle (as well as stars with no displacement information) are assumed to be cluster members and have been included in the analysis, while those beyond the circle are considered as field contaminants. The red and black squares mark the cluster-member and the field-contaminant BSSs, respectively.

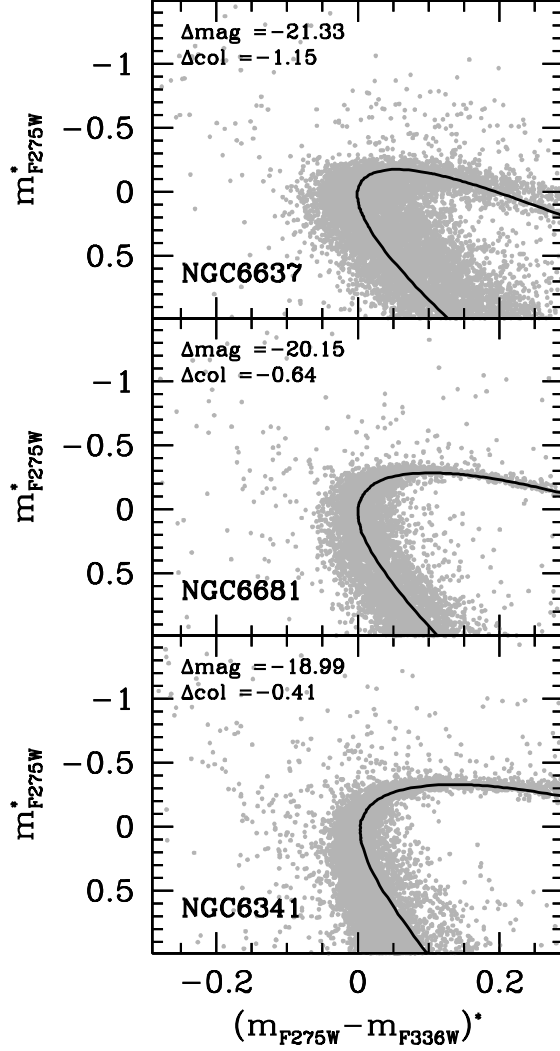


Fig. 2.— Normalized CMD zoomed in the MS-TO region for three clusters (namely NGC 6637, NGC 6681, NGC 6341) belonging to the three metallicity groups defined in the text (from top to bottom, metal rich, metal intermediate and metal poor). The adopted 12-Gyr isochrone (from the BaSTI database) is shown as a solid line, and shifts in color and magnitude have been adopted to locate the MS-TO at $m_{F275W}^* = 0$ and $(m_{F275W} - m_{F336W})^* = 0$ are labelled in each panel.

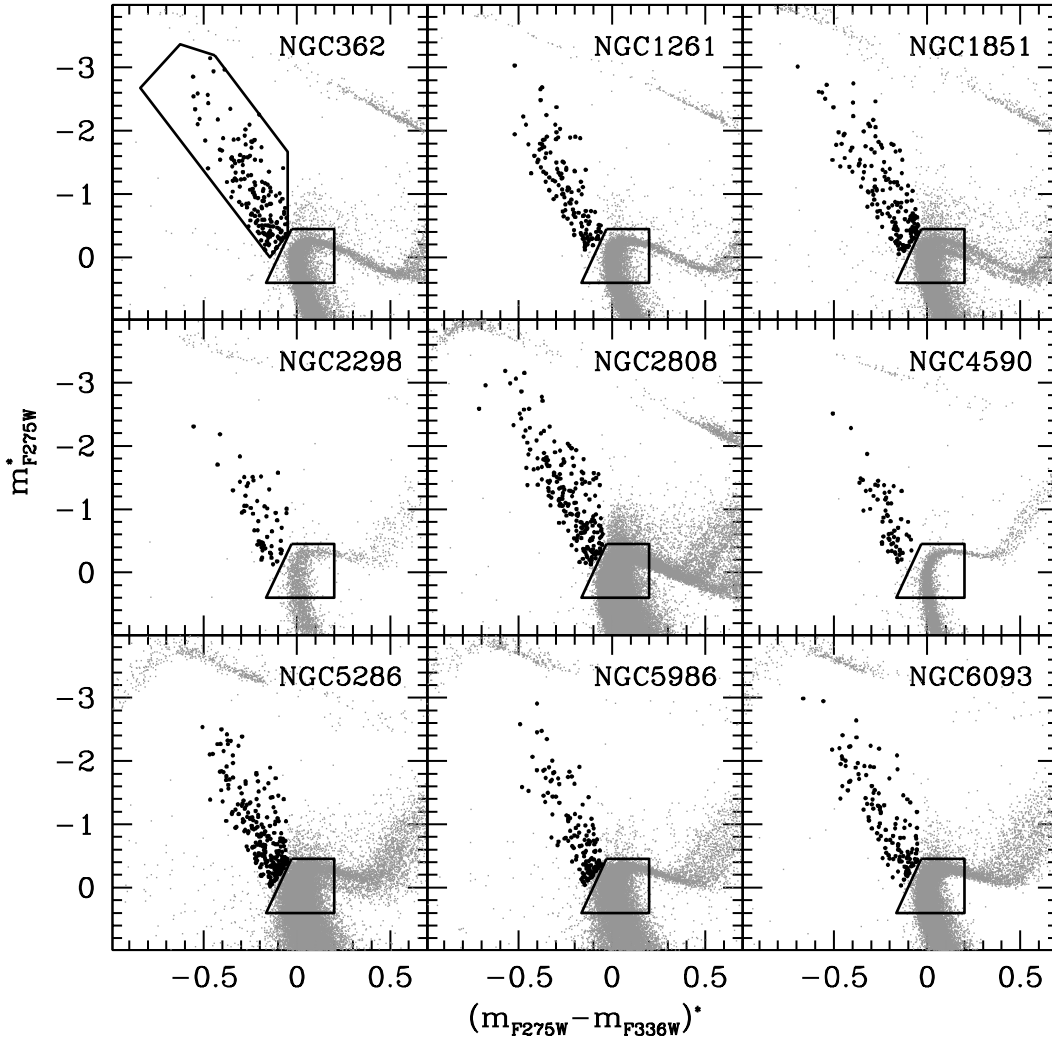


Fig. 3.— The sample of BSSs (black dots) identified in each cluster is shown in the n-CMD. The BSS selection box is drawn in the first panel, the one adopted for the MS-TO population is marked for all clusters.

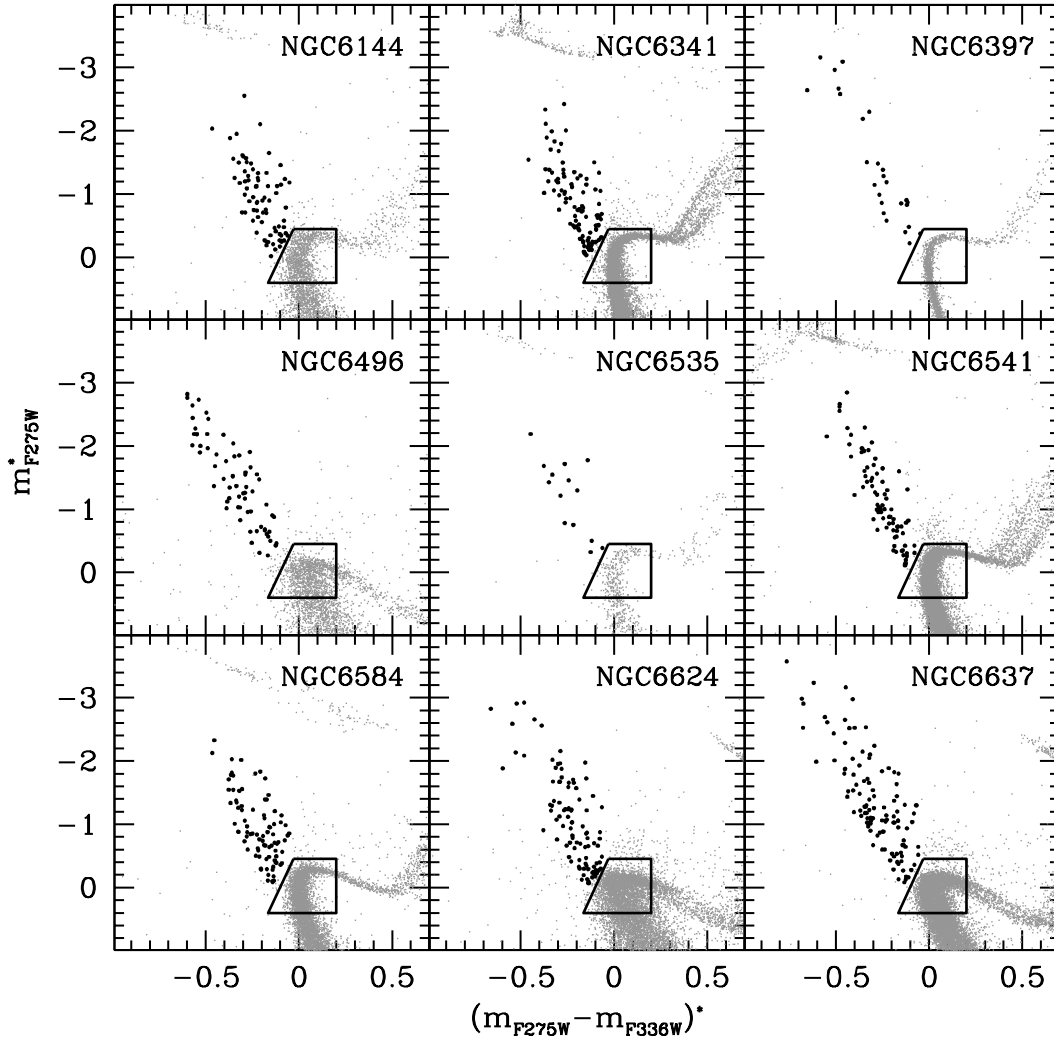


Fig. 4.— As in Figure 3.

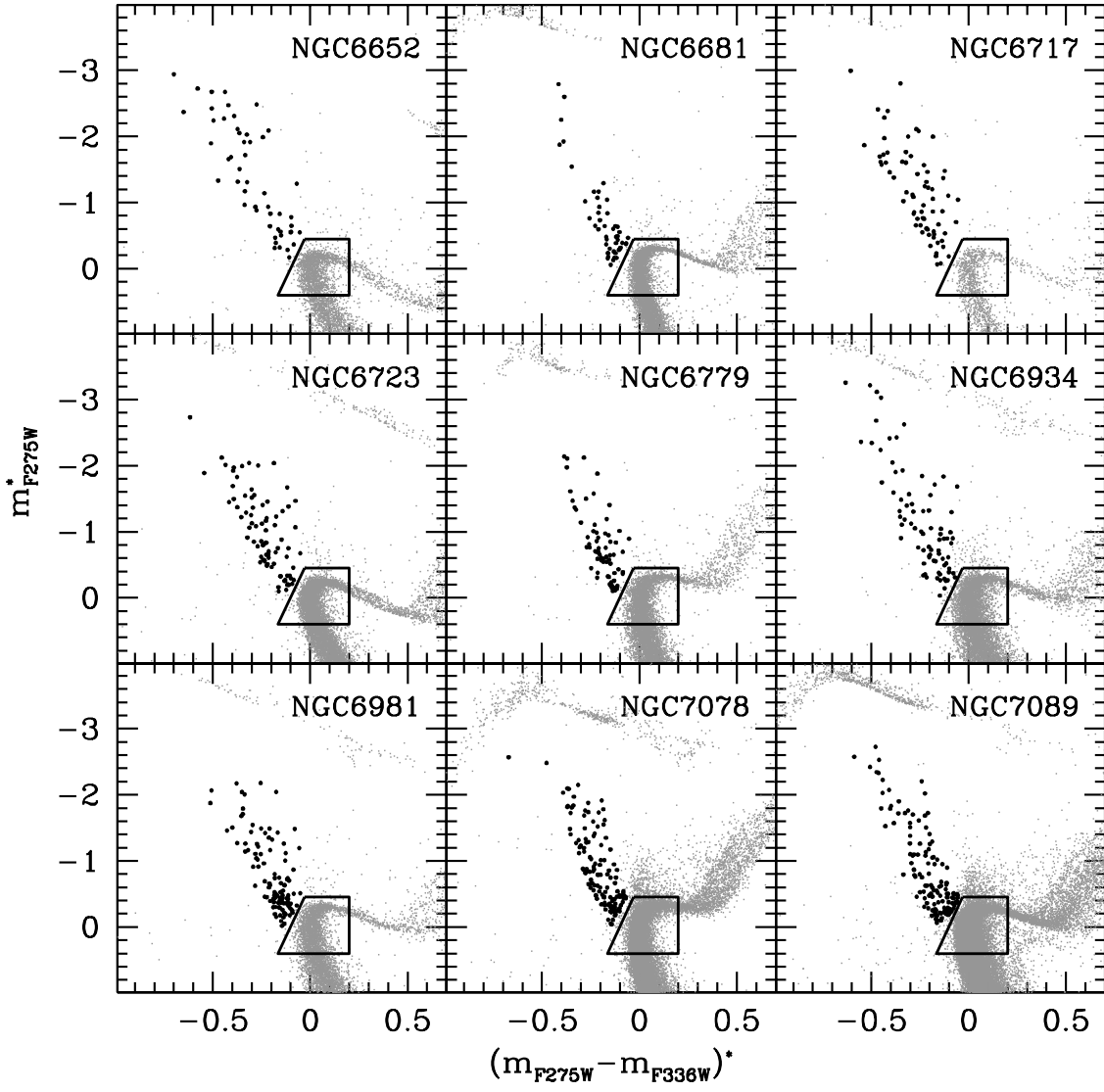


Fig. 5.— As in Figure 3.

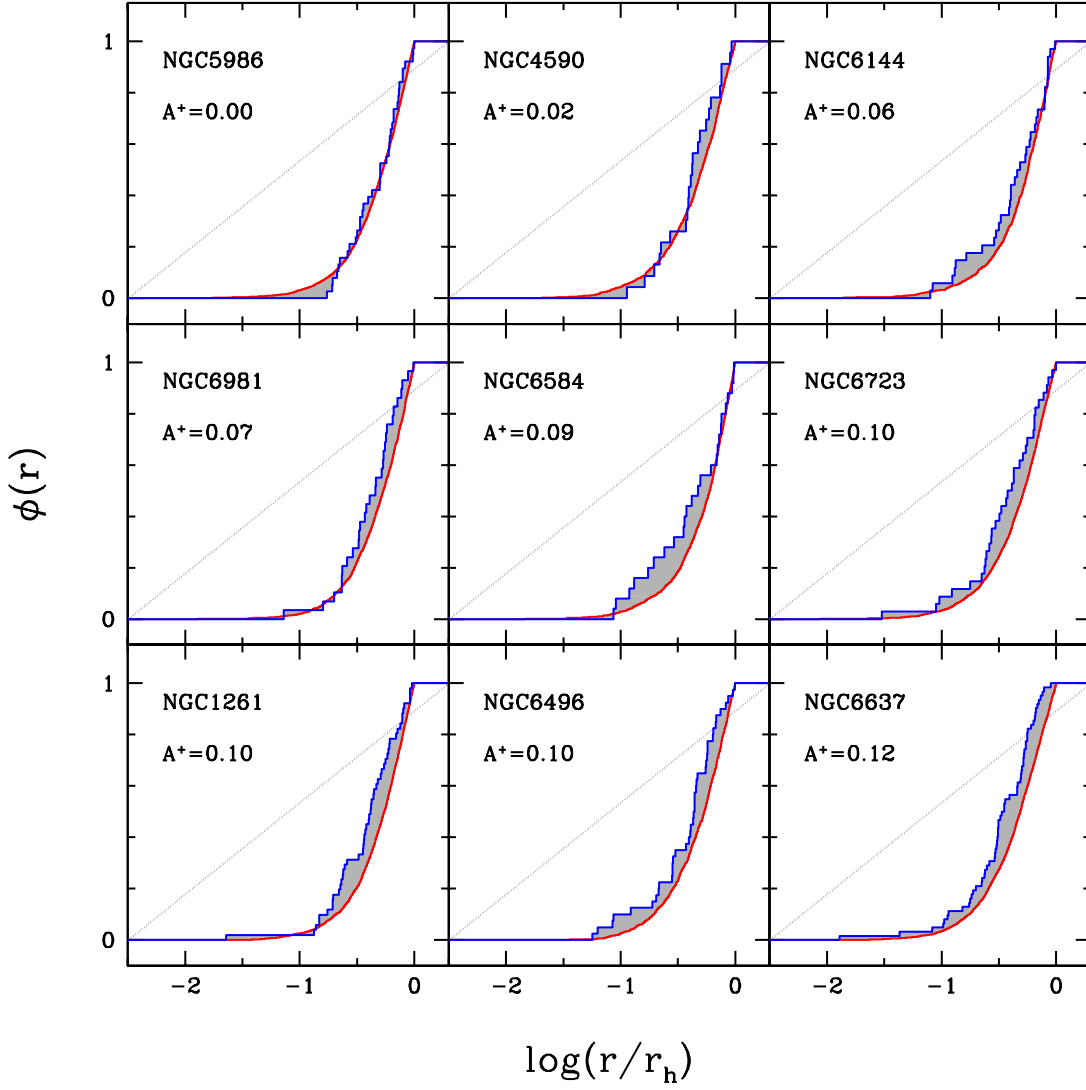


Fig. 6.— Cumulative radial distributions of BSSs (blue line) and REF stars (red line) in the nine GCs with the smallest values of $A_{r_h}^+$. By construction (see Sect. 3), the cumulative radial distributions are normalized to unity at r_h . The size of the area between the two curves (shaded in grey) corresponds to the labelled value of $A_{r_h}^+$ (see also Table 1). Clusters are ranked in terms of increasing value of $A_{r_h}^+$.

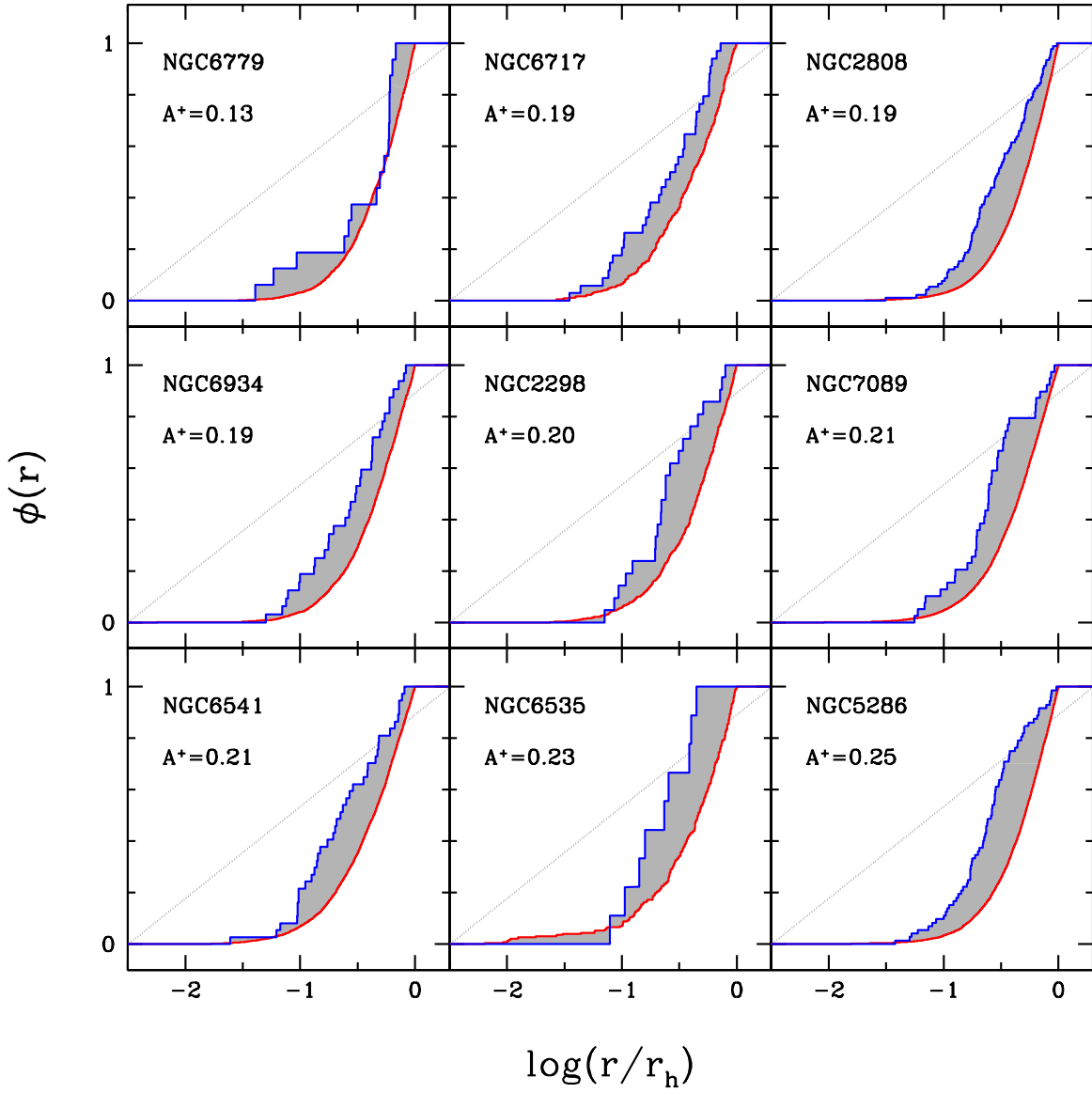


Fig. 7.— As in Figure 6, for the nine GCs with increasingly larger value of A^+_{rh} .

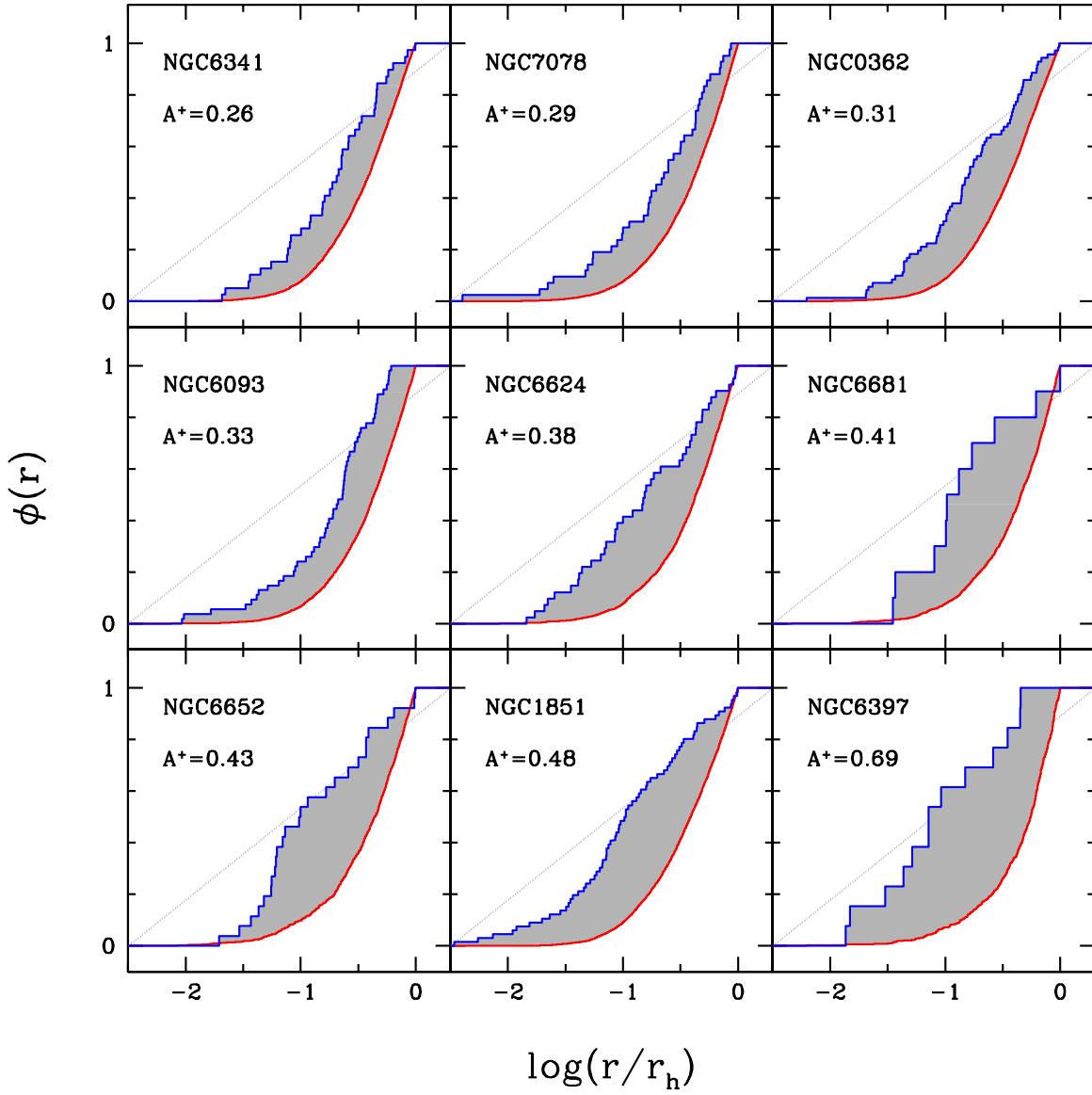


Fig. 8.— As in Figure 6, for the remaining nine GCs, those with the largest values of A^+_{rh} .

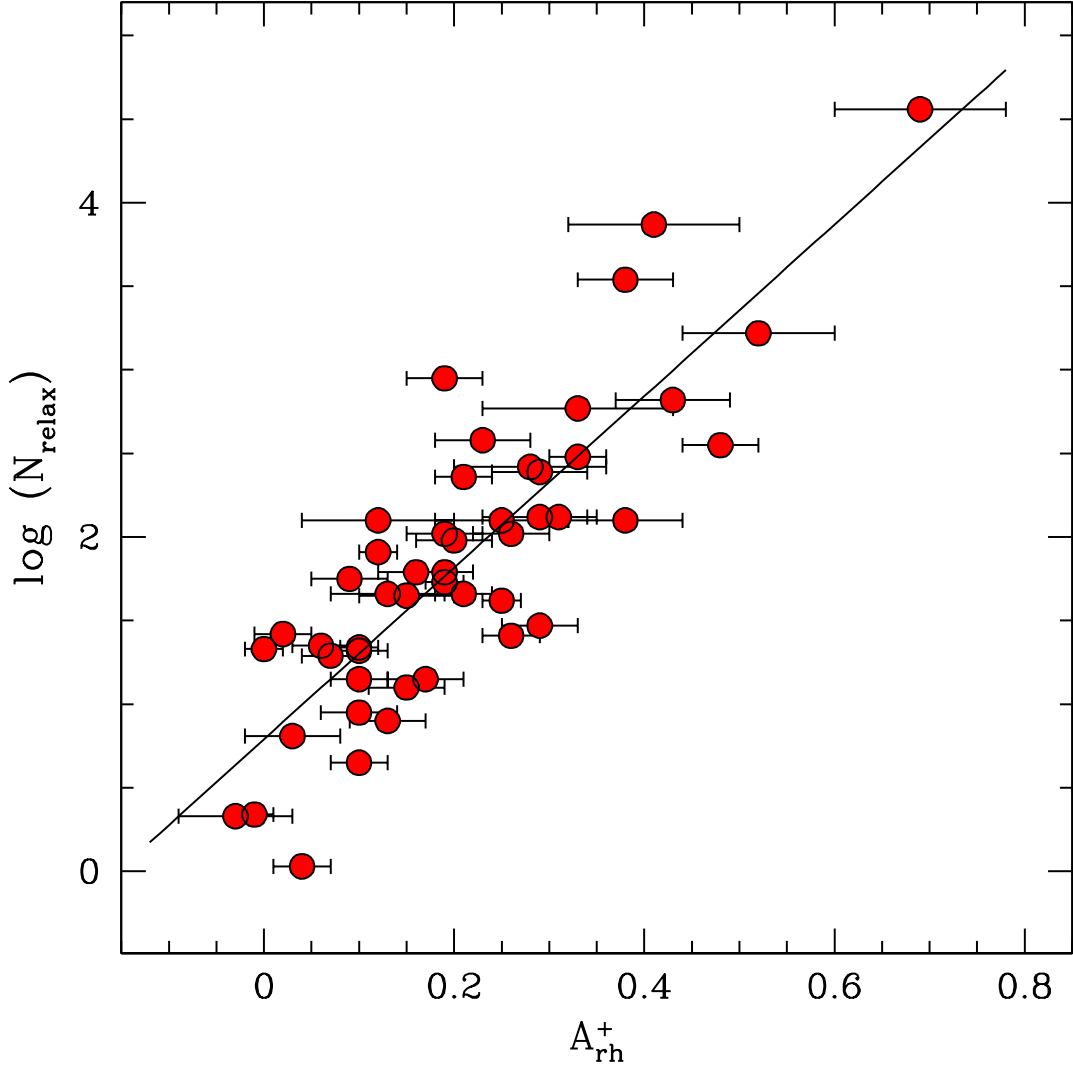


Fig. 9.— Relation between A_{rh}^+ and $\log(N_{relax})$ for the entire sample of 48 GCs. The parameter $N_{relax} = t_{GC}/t_{rc}$ quantifies the number of current central relaxation times occurred since cluster formation. The tight relation between these two parameters demonstrates that the segregation level of BSSs measured by A^+ can be used to evaluate the level of dynamical evolution experienced by the parent cluster.

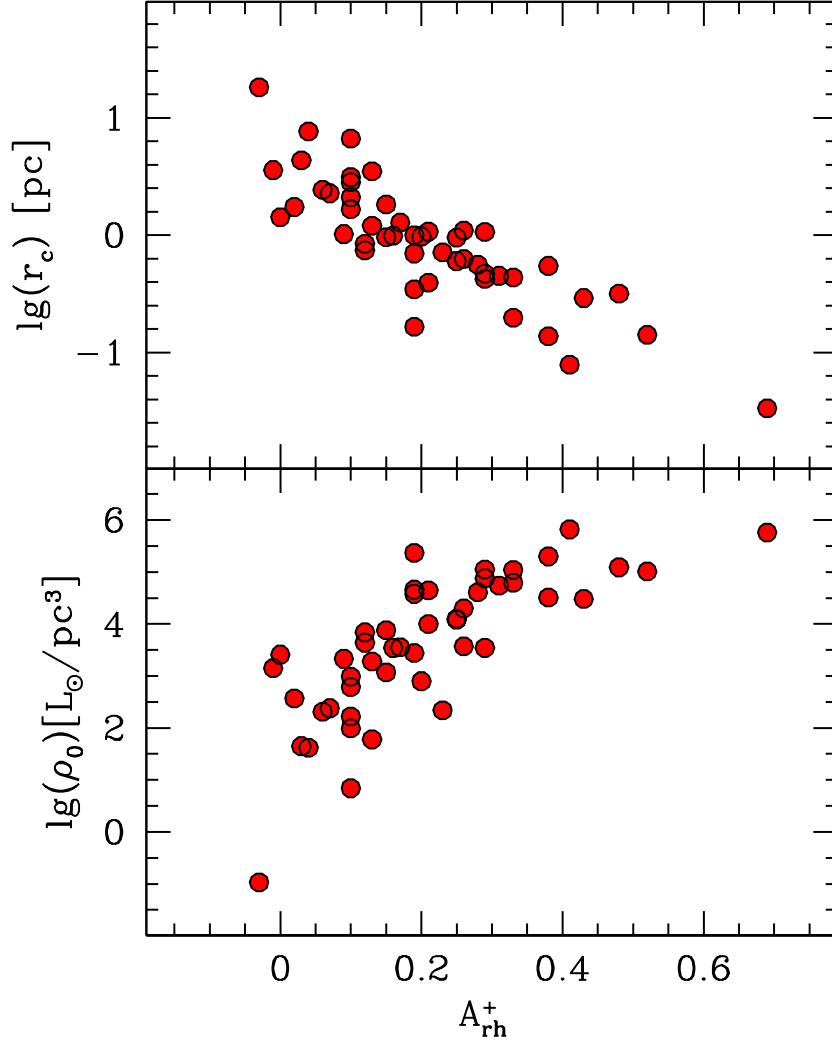


Fig. 10.— Relation between A_{rh}^+ and two physical parameters that are expected to change with the long-term dynamical evolution of GCs: the core radius (*upper panel*) and the central luminosity density (*lower panel*), both taken from Harris (1996).

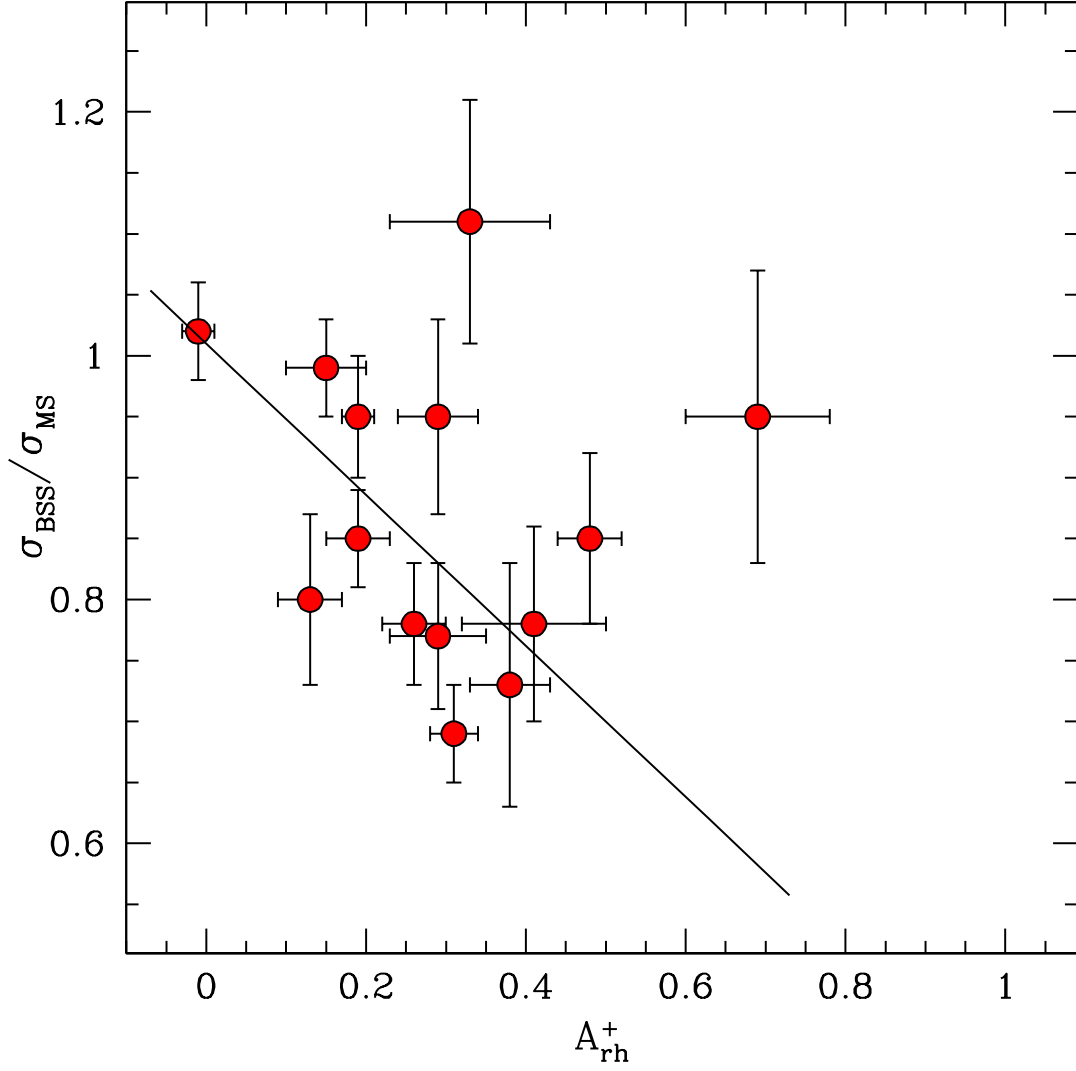


Fig. 11.— Relation between A_{rh}^+ and the ratio $\alpha \equiv \sigma_{BSS}/\sigma_{MS-TO}$ between the BSS velocity dispersion and that of stars near the top of the MS for the 14 GCs in common with Baldwin et al. (2016). The best-fit relation quoted in equation 3 is shown as a solid line.

| Name | c | r_c | r_h | $\log(t_{rc})$ | A_{rh}^+ | ϵ_{A^+} |
|---------|------|-------|-------|----------------|------------|------------------|
| NGC5986 | 1.23 | 28.2 | 58.8 | 8.75 | -0.00 | 0.02 |
| NGC4590 | 1.41 | 34.8 | 90.6 | 8.66 | 0.02 | 0.03 |
| NGC6144 | 1.55 | 56.4 | 97.8 | 8.73 | 0.06 | 0.03 |
| NGC6981 | 1.21 | 27.6 | 55.8 | 8.79 | 0.07 | 0.03 |
| NGC6584 | 1.47 | 15.6 | 43.8 | 8.33 | 0.09 | 0.04 |
| NGC6723 | 1.11 | 49.8 | 91.8 | 8.93 | 0.10 | 0.03 |
| NGC1261 | 1.16 | 21.0 | 40.8 | 8.74 | 0.10 | 0.02 |
| NGC6496 | 1.18 | 35.6 | 93.6 | 8.76 | 0.10 | 0.03 |
| NGC6637 | 1.38 | 19.8 | 50.4 | 8.17 | 0.12 | 0.02 |
| NGC6779 | 1.38 | 26.4 | 66.0 | 8.42 | 0.13 | 0.06 |
| NGC6717 | 1.71 | 8.0 | 45.0 | 7.13 | 0.19 | 0.04 |
| NGC2808 | 1.56 | 15.0 | 48.0 | 8.35 | 0.19 | 0.02 |
| NGC6934 | 1.53 | 13.2 | 41.4 | 8.29 | 0.19 | 0.03 |
| NGC2298 | 1.38 | 18.6 | 58.8 | 8.10 | 0.20 | 0.04 |
| NGC7089 | 1.57 | 15.4 | 66.3 | 8.42 | 0.21 | 0.03 |
| NGC6541 | 1.86 | 10.8 | 63.6 | 7.72 | 0.21 | 0.03 |
| NGC6535 | 1.56 | 17.5 | 73.4 | 7.50 | 0.23 | 0.05 |
| NGC5286 | 1.41 | 16.8 | 43.8 | 8.46 | 0.25 | 0.02 |
| NGC6341 | 1.74 | 14.6 | 85.0 | 8.06 | 0.26 | 0.04 |
| NGC7078 | 2.29 | 8.4 | 60.0 | 7.69 | 0.29 | 0.05 |
| NGC0362 | 1.73 | 13.0 | 73.8 | 7.96 | 0.31 | 0.03 |
| NGC6093 | 1.74 | 7.0 | 40.6 | 7.60 | 0.33 | 0.03 |
| NGC6624 | 2.50 | 3.6 | 49.2 | 6.54 | 0.38 | 0.05 |
| NGC6681 | 2.50 | 1.8 | 42.6 | 6.21 | 0.41 | 0.09 |
| NGC6652 | 1.80 | 6.0 | 28.8 | 7.26 | 0.43 | 0.06 |
| NGC1851 | 1.95 | 5.4 | 51.0 | 7.53 | 0.48 | 0.04 |
| NGC6397 | 2.50 | 3.0 | 174.0 | 5.52 | 0.69 | 0.09 |

Table 1: Structural/dynamical parameters and values of A_{rh}^+ for the 27 program clusters: concentration parameter (column 2), core and half-mass radii in arcseconds (columns 3 and 4, respectively), logarithm of the central relaxation time in Gyr (column 5), derived value of A_{rh}^+ and its error (columns 6 and 7). The structural parameters are from Mocchi et al. (2013), L16, Cadelano et al. (2017), and Harris (1996) if not available in the previous studies, but for NGC 6717 and NGC 6535 and NGC 6496 for which we performed new determinations (Ferraro et al. 2018, in preparation). Clusters are ordered in terms of increasing value of A_{rh}^+ .